Symmetrical PLL for SISO Impedance Modeling and Enhanced Stability in Weak Grids

Yang, Dongsheng; Wang, Xiongfei; Liu, Fangcheng; Xin, Kai; Liu, Yunfeng; Blaabjerg, Frede

Published in:
IEEE Transactions on Power Electronics

DOI (link to publication from Publisher):
10.1109/TPEL.2019.2917945

Publication date:
2020

Document Version
Publisher's PDF, also known as Version of record

Symmetrical PLL for SISO Impedance Modeling and Enhanced Stability in Weak Grids

Dongsheng Yang, *Member, IEEE*, Xiongfei Wang, *Senior Member, IEEE*, Fangcheng Liu, Kai Xin, Yunfeng Liu, and Frede Blaabjerg, *Fellow, IEEE*

***Abstract*—This paper proposes a symmetrical phase-locked loop (PLL) that can eliminate the frequency-coupling terms caused by the asymmetric dynamics of conventional PLLs. In the approach, a concept of complex phase angle vector with both real and imaginary phase components is introduced, which enables to control the direct- and quadrature-axis components with symmetrical dynamics. The small-signal impedance model that characterizes the dynamic effect of the symmetrical PLL on the current control loop is also derived, which, differing from the conventional multiple-input multiple-output impedance matrix, is in a single-input single-output (SISO) form based on complex transfer functions. This SISO representation allows for a design-oriented analysis. Moreover, the undesired sub-synchronous oscillation caused by the conventional asymmetrical PLL can be avoided, and the classical SISO impedance shaping can be utilized to cancel the negative resistor behavior caused by PLL; thus can greatly enhance the grid synchronization stability under weak grid conditions. The effectiveness of the theoretical analysis is validated by experimental tests.**

***Index Terms*—Frequency coupling, impedance modeling, multiple-input multiple-output (MIMO), phase-locked loop (PLL), single-input single-output (SISO) impedance shaping.**

I. Introduction

OVER the past decade, power electronic converters are increasingly used as the grid interface for renewable power sources and energy-efficient loads. Despite the advantages of power converters in terms of high controllability and improved efficiency, various resonance and stability issues are also introduced by the interactions between wideband control dynamics of converters, passive power filters, as well as the grid impedance [1].

It has been reported that the phase-locked loop (PLL) used for grid synchronization may bring a significant impact on the stability of the grid-connected converter, especially under the weak grid condition when the local voltage measured by the PLL is more influenced by the converter itself than by the grid voltage at the remote terminal [2]–[4]. To effectively address these challenges, the impedance-based approach has recently been developed in [5], which not only provides an intuitive insight of the interactions among the power converters but also enables to reshape output impedance for stabilizing the power system. With this method, a grid-connected converter, including the control system and the passive filter, is represented by a Thevenin/Norton equivalent circuit, where the output impedance/admittance allows analyzing the dynamic interaction between the converter and external grid/load impedance [6]. In order to perform the stability analysis in different frames directly, different linearization methods are utilized to establish the impedance model of the converter, resulting in the *dq*-frame impedance model [7], [8] and the $\alpha\beta$-frame impedance model [9]. The mathematical relations between the two models have recently been established in [10], and it is revealed that all the models have the same stability implications.

Since only the *q*-axis voltage is controlled for the phase tracking in the synchronous reference frame (SRF) PLL, the asymmetrical cross couplings between *d* and *q* axes in *dq*-frame impedance model, and introduce frequency couplings when the dynamics of PLL are included into the grid-converter interaction [7]. Transfer matrices with cross couplings between the *d*- and *q*-axis components are needed for the stability analysis

Due to the inherent asymmetry of the SRF-PLL, both the *dq*-frame and $\alpha\beta$-frame impedance models have to be represented by the impedance matrices to capture the asymmetrical dynamics [10]. Consequently, the generalized Nyquist criterion has to be utilized for the stability assessment of this multi-input multi-output (MIMO) dynamic system. To facilitate the stability analysis and control design, some research efforts have been made to approximate the MIMO system to a single-input and single-output (SISO) system [11]. However, only the symmetric MIMO system can be strictly represented by a SISO complex transfer function [12]. Although the magnitudes of cross-coupling components in asymmetric MIMO matrix are small in some cases, ignoring them can still lead to inaccurate stability implications [7], [13]. Moreover, the asymmetric dynamics of PLL characterized by the asymmetric MIMO matrix result in the frequency coupling effects in sequence domain, i.e., the one single-frequency perturbation imposed on the grid-connected converter will generate responses at two frequencies that are separated by twice fundamental frequency ($2f_1$) [9]. This frequency-coupling effect tends to introduce a sideband oscillation below

Manuscript received November 30, 2018; revised February 18, 2019; accepted May 14, 2019. Date of publication June 16, 2019; date of current version November 12, 2019. Recommended for publication by Associate Editor F. W. Fuchs. *(Corresponding author: Xiongfei Wang.)*

D. Yang, X. Wang, and F. Blaabjerg are with the Department of Energy Technology, Aalborg University, Aalborg DK-9220, Denmark (e-mail: doy@et.aau.dk; xwa@et.aau.dk; fbl@et.aau.dk).

F. Liu, K. Xin, and Y. Liu are with the Watt Laboratory, Central Research Institute, Huawei Technologies Co. Ltd., Shanghai 201206, China (e-mail: formula.liu@huawei.com; kai.xin@huawei.com; yf.liu@huawei.com).

Color versions of one or more of the figures in this paper are available online at http://ieeexplore.ieee.org.

Digital Object Identifier 10.1109/TPEL.2019.2917945

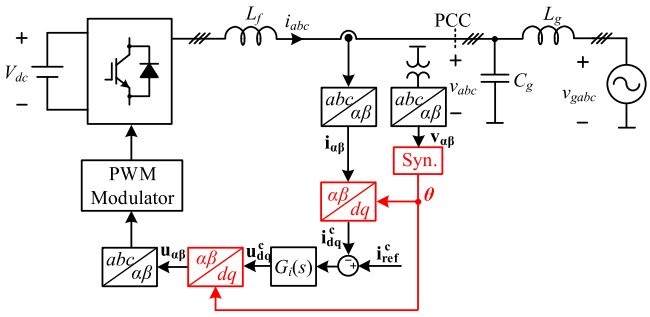

Fig. 1. One-line diagram of a three-phase grid-connected VSC.

the fundamental frequency, which can easily propagate in the power system and even trigger the sub-synchronous oscillations (SSO) together with the traditional power plant [10]. It was reported that a low-frequency resonance in a wind farm resulted in the shaft torsional vibration protection and thereby the generator tripping in the thermal generation plant 200 km away [14]. Therefore, the elimination of such a frequency coupling dynamic and the associated low-frequency resonances are deemed critical to the safe operation of the modern power system.

In this paper, a symmetrical PLL is proposed to remove the frequency-coupling effect of the conventional asymmetrical PLLs. The concept of the complex phase angle, i.e., phase angle with both the real part and imaginary part, is introduced to symmetrically capture the dynamics of the grid voltage in *q* and *d* axes, respectively. Moreover, the new *dq* reference frame is also defined to detect the complex phase angle, which can still guarantee the synchronization and power control under weak grids. The significance of the proposed symmetrical PLL can be summarized as the following.

1) The sub-synchronous oscillation hazard caused by the conventional PLL is eliminated.
2) The MIMO system is simplified into SISO complex transfer functions, which greatly facilitates the stability analysis.
3) SISO impedance shaping can be implemented to enhance the grid synchronization stability under the weak grid condition.

II. System Description

Fig. 1 shows a simplified one-line diagram of a three-phase grid-connected voltage-source converter (VSC). The dc-link voltage $V_{\rm dc}$ is assumed to be constant, and an *LC*-type grid impedance is considered in this paper. The current control is realized with PI controller $G_i(s)$ in the *dq*-frame. A synchronization unit is used to synchronize the voltage at the point of common connection (PCC) to the grid.

For clarity, the italic letters are used in this paper to denote the real vectors, e.g., $x_{\alpha\beta} = [x_\alpha, x_\beta]^T$ and $x_{dq} = [x_d, x_q]^T$ for the variables x in the $\alpha\beta$ and *dq* frames, respectively. The corresponding complex vectors are represented by the bold letters, e.g., $\boldsymbol{x}_{\alpha\beta} = x_\alpha + jx_\beta$, and $\boldsymbol{x}_{\mathbf{dq}} = x_d + jx_q$. The relationship between two real vectors can be represented by MIMO transfer function matrix $G_m(s)$, i.e.,

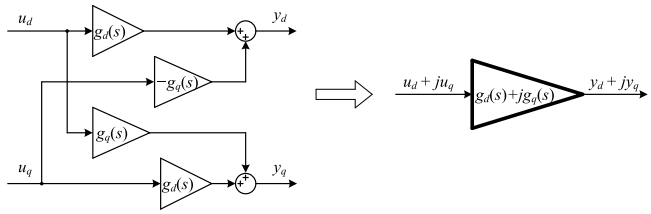

Fig. 2. Equivalence of symmetrical MIMO transfer function matrix and SISO complex transfer function.

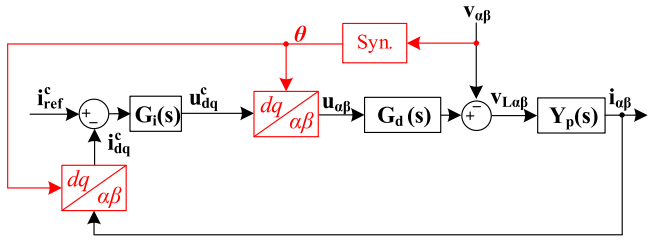

Fig. 3. Block diagram of the *L*-filtered three-phase VSC.

$$\begin{bmatrix} y_d \\ y_q \end{bmatrix} = \underbrace{\begin{bmatrix} g_{dd}(s) & g_{dq}(s) \\ g_{qd}(s) & g_{qq}(s) \end{bmatrix}}_{G_m(s)} \begin{bmatrix} u_d \\ u_q \end{bmatrix}. \tag{1}$$

As shown in Fig. 2, when the MIMO transfer function matrix $G_m(s)$ is symmetrical, i.e., $g_d(s) = g_{dd}(s) = g_{qq}(s)$ and $g_q(s) = g_{qd}(s) = -g_{dq}(s)$, it can be equivalently transformed into SISO complex transfer function **G(s)** by replacing the input/output real vectors with corresponding complex vectors [12], i.e.,

$$\begin{bmatrix} y_d \\ y_q \end{bmatrix} = \underbrace{\begin{bmatrix} g_d(s) & -g_q(s) \\ g_q(s) & g_d(s) \end{bmatrix}}_{G_m(s)} \begin{bmatrix} u_d \\ u_q \end{bmatrix}$$

$$\Leftrightarrow y_d + jy_q = \underbrace{[g_d(s) + jg_q(s)]}_{\mathbf{G(s)}} (u_d + ju_q). \tag{2}$$

Fig. 3 depicts the block diagram of the *L*-filtered three-phase VSC, where $\mathbf{G_d(s)}$ represents the time delay of 1.5 times the switching period, which is introduced by the digital computation and pulsewidth modulator; $\mathbf{Y_p(s)}$ is the admittance of the converter-side filter inductor. In $\alpha\beta$-frame, they can be expressed as

$$\mathbf{G_d(s)} = e^{-1.5T_s s} \tag{3}$$

$$\mathbf{Y_p(s)} = \frac{1}{sL_f}. \tag{4}$$

III. Asymmetrical Dynamic Effect of SRF-PLL Based Grid Synchronization

The synchronization unit in Fig. 1 can be realized by the conventional SRF-PLL, and its control block diagram is depicted in

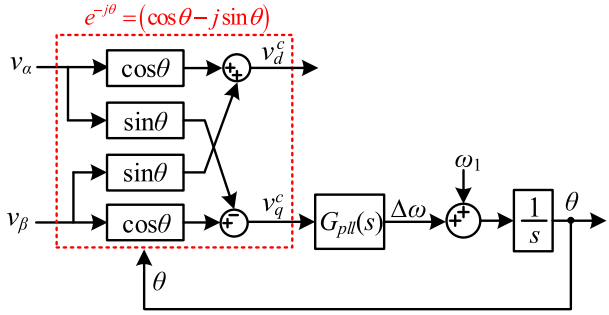

Fig. 4. Control block diagram of the conventional SRF-PLL.

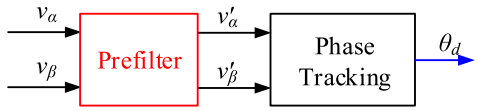

Fig. 5. General block diagram of the filtered SRF-PLLs.

Fig. 4, where ω_1 is the grid fundamental frequency. The $\alpha\beta$/dq-transformation is used for the phase detection, and it can be expressed in either complex vector form or real vector, as

$$\mathbf{v_{dq}^c} = e^{-j\theta}\cdot\mathbf{v}_{\alpha\beta} \tag{5}$$

$$\begin{bmatrix} v_d^c \\ v_q^c \end{bmatrix} = \begin{bmatrix} \cos\theta & \sin\theta \\ -\sin\theta & \cos\theta \end{bmatrix} \begin{bmatrix} v_\alpha \\ v_\beta \end{bmatrix}. \tag{6}$$

The mathematical equivalence of the MIMO transfer function matrix can be equivalently transferred into the SISO complex transfer function when the transfer function meets characteristics.

The q-axis voltage is regulated by a PI controller $G_{pll}(s)$ for the phase tracking. Since only the q-axis voltage is utilized in SRF-PLL, this control structure will result in asymmetric dynamics to the d and q axes.

In fact, not only the basic SRF-PLL, but also the filtered SRF-PLLs will introduce the frequency coupling effects. The general block diagram of these PLLs can be depicted by Fig. 5, where the prefilter and improved phase tracking algorithms can be used to improve the phase tracking performance when the PCC voltage suffers from background harmonics, unbalances, or sudden phase jump, etc. In order to extract the phase angle accurately under the distorted and unbalanced grid conditions, the PCC voltage can be filtered first through the prefilter to detect its fundamental positive-sequence component. The typical prefilters include the positive-sequence filter based on the generalized integrator [15], the quadrature PLL [16], the adaptive filter based on the second-order generalized integrator [17]–[19], the complex coefficient prefilter [20], [21], and the prefilters based on the delayed signal cancellation [22]–[24]. Moreover, the modified phase tracking algorithm with in-loop filters [25]–[26] can be used to further to enhance the phase tracking the performance of SRF-PLL against the grid voltage distortions.

Despite many filtered SRF-PLLs reported in the literature for grid-connected converters to achieve the accurate phase and frequency tracking under different grid voltage disturbances, most of those schemes can be unified as the asymmetrical PLL [27], which tends to cause the frequency-coupled oscillations in weak power grids [28]. In a more general perspective, the root cause of asymmetrical dynamics of these filtered-SRF-PLLs stems from their dimensionality collapse, i.e., the input is two-dimensional (2-D) vector, whereas the output is 1-D scalar, which destroys the symmetry.

Assumed that the one-dimensional phase angle obtained from filtered SRF-PLL is denoted as θ_d, and it can be equivalently decomposed into positive- and negative-sequence of the complex phase angles, i.e.,

$$\theta_d = \frac{1}{2}\underbrace{(\theta_d + j\theta_q)}_{\boldsymbol{\theta}_+} + \frac{1}{2}\underbrace{(\theta_d - j\theta_q)}_{\boldsymbol{\theta}_-}. \tag{7}$$

In (7), the concept of complex phase angle is introduced, including both d- and q-axis components. The d-axis component θ_d has the same concept as the conventional phase angle, whereas the q-axis component θ_q defines the deviation of the PCC voltage magnitude from its nominal value V_1. The expression of the positive complex phase angle can be expressed as

$$e^{j\theta_+} = e^{j(\theta_d + j\theta_q)} = e^{j\theta_d}\cdot e^{-\theta_q}. \tag{8}$$

So, if the $\theta_q = 0$, then $e^{-\theta_q} = 1$, which indicates that PCC voltage magnitude is equal to its nominal value V_1. If $\theta_q > 0$, then $e^{-\theta_q} < 1$, which means that the PCC voltage magnitude is less than its nominal value V_1 and vice versa. Therefore, with the concept of complex phase angle, it is able to characterize the dynamics of both magnitude and phase angle of PCC voltage.

According to (7), for a single-frequency positive-sequence PCC voltage perturbation in the $\alpha\beta$-frame, the response of the output converter current seen from the PCC will be composed of two components at different frequencies [10], i.e.,

$$\underset{80\text{Hz}}{\boldsymbol{\Delta}\mathbf{v}_{\alpha\beta+}} \rightarrow \underset{30\text{Hz}}{\boldsymbol{\Delta}\mathbf{v}_{\mathbf{dq}+}} \rightarrow \underset{30\text{Hz}}{\Delta\theta_d} \begin{cases} \underset{30\text{Hz}}{\boldsymbol{\Delta}\theta_+} \rightarrow \underset{30\text{Hz}}{\Delta\mathbf{i}_{\mathbf{dq}+}} \rightarrow \underset{80\text{Hz}}{\boldsymbol{\Delta}\mathbf{i}_{\alpha\beta+}} \\ \underset{-30\text{Hz}}{\boldsymbol{\Delta}\theta_-} \rightarrow \underset{-30\text{Hz}}{\Delta\mathbf{i}_{\mathbf{dq}-}} \rightarrow \underset{20\text{Hz}}{\boldsymbol{\Delta}\mathbf{i}_{\alpha\beta-}}\cdot e^{j2\omega_1 t} \end{cases}. \tag{9}$$

The SSO caused by the frequency-coupling effect is illustrated by the following example: assuming that the grid fundamental frequency is 50 Hz and the system contains an undamped oscillation at 80 Hz in the $\alpha\beta$-frame, then this oscillation frequency will be shifted to 30 Hz in the dq-frame. Due to the frequency-coupling effect of the PLL, another oscillation will be generated in the negative sequence, which can be represented by a three-phase vector at the negative frequency (-30 Hz). Consequently, a sub-synchronous oscillation would be observed at 20 Hz in the $\alpha\beta$-frame, due to the frequency shift of the inverse Park transformation. Since the additional oscillation frequency aroused by the frequency coupling is in the negative sequence in the dq-frame, it tends to be shifted to a lower frequency that is below the grid fundamental frequency in the $\alpha\beta$-frame, especially under the weak grid condition.

Moreover, this frequency-coupling effect also complicates the converter dynamics. The admittance matrix with the less

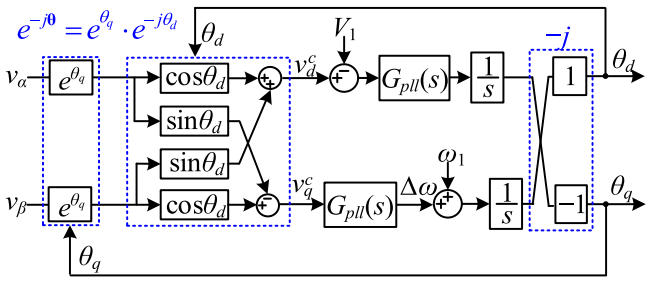

Fig. 6. Control block diagram of the proposed symmetrical PLL.

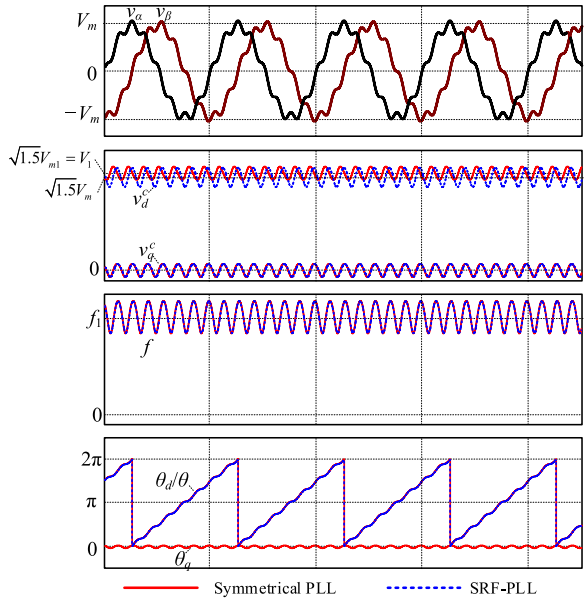

Fig. 7. Operational waveforms of the proposed symmetrical PLL and the SRF-PLL.

physical insight has to be used [10] to represent this frequency-coupling dynamics, which makes it difficult to perform the stability analysis and damping control.

In the next section, the symmetrical PLL will be proposed to get rid of the frequency coupling effects by tracking the complex phase angle.

IV. Symmetrical PLL

To address the frequency-coupling effects of asymmetrical PLLs, the concept of the complex phase angle, i.e., phase angle with both the real and imaginary parts, is introduced to symmetrically capture the dynamics of the grid voltage in *q* and *d* axes, respectively. Moreover, the new *dq* reference frame is also defined accordingly to detect the complex phase angle. The control scheme of the proposed symmetrical PLL is shown in Fig. 6. Similar to the SRF-PLL, the input of symmetrical PLL is the PCC voltages in the stationary $\alpha\beta$-frame, its output, however, is a complex vector rather than a real number, which includes both the d and q components, i.e., $\theta = \theta_d + j\theta_q$. Moreover, both d- and q-axis voltages are utilized for phase tracking. Hence, the control structure is symmetrical, which can remove the frequency couplings.

Due to the usage of the complex phase angle θ**,** the new *dq*-frame is defined and its $\alpha\beta$*/dq*-transformation rule in Fig. 1 should be modified accordingly. In complex vector form, it can be expressed as

$$\mathbf{x_{dq}} = e^{-j\theta} \cdot \mathbf{x}_{\alpha\beta} = e^{-j(\theta_d + j\theta_q)} \cdot \mathbf{x}_{\alpha\beta}. \tag{10}$$

In real vector form, it can also be expressed as

$$\begin{bmatrix} x_d \\ x_q \end{bmatrix} = e^{\theta_q} \begin{bmatrix} \cos\theta_d & \sin\theta_d \\ -\sin\theta_d & \cos\theta_d \end{bmatrix} \begin{bmatrix} x_\alpha \\ x_\beta \end{bmatrix}. \tag{11}$$

Likewise, the *dq*/$\alpha\beta$ transformation rule using complex phase angle θ can be expressed in complex vector form and real vector form as

$$\mathbf{x}_{\alpha\beta} = e^{j\theta} \cdot \mathbf{x}_{dq} = e^{j(\theta_d + j\theta_q)} \cdot \mathbf{x}_{dq} \tag{12}$$

$$\begin{bmatrix} x_\alpha \\ x_\beta \end{bmatrix} = e^{-\theta_q} \begin{bmatrix} \cos\theta_d & -\sin\theta_d \\ \sin\theta_d & \cos\theta_d \end{bmatrix} \begin{bmatrix} x_d \\ x_q \end{bmatrix}. \tag{13}$$

Fig. 7 illustrates the operational waveforms for the SRF-PLL and the proposed symmetrical PLL, where the PCC voltage in both cases contains small perturbations, and meanwhile its magnitude V_m is intentionally set to 0.9 of its nominal value V_{m1} to reveal the difference of the two PLLs. It is clear that the output of the symmetrical PLL at *d*-axis θ_d, is exactly the same as that of SRF-PLL θ. The *q* component of symmetrical PLL θ_q provides additional information of magnitude variation of PCC voltage by regulating v_d^c to its nominal value V_1, which helps us to remove the frequency couplings.

V. Frequency Decoupled Dynamics of the Symmetrical PLL

A. Modeling of Symmetrical PLL Dynamics

Following the small-signal modeling of the SRF-PLL [5], two *dq*-frames are defined to model the frequency-decoupled dynamics of the proposed symmetrical PLL. One is the grid *dq*-frame that is defined by the phase angle of the fundamental positive-sequence PCC voltage **v,** denoted as θ_1. The other is the converter *dq*-frame, which is based on the complex phase angle vector obtained from the symmetrical PLL, denoted as θ. Vectors in the converter *dq*-frame are denoted with the superscript c in the following analysis. Given a perturbation on the PCC voltage in the grid *dq*-frame $\mathbf{\Delta v_{dq}}$, the PCC voltage in the stationary $\alpha\beta$-frame can be expressed as

$$\mathbf{v}_{\alpha\beta} = v_\alpha + jv_\beta = (V_1 + \mathbf{\Delta v_{dq}})\, e^{j\theta_1} \tag{14}$$

where V_1 is the steady-state PCC voltage aligned to the *d*-axis, i.e., the steady-state PCC voltage vector, $\mathbf{V_{dq}1} = V_1 + j0$. The response of the detected complex phase angle vector θ to the voltage perturbation can be given as

$$\theta = \theta_1 + \Delta\theta. \tag{15}$$

According to the modified *dq* transformation given in (10), the PCC voltage at converter *dq*-frame can be given as

$$\mathbf{v_{dq}^c} = \mathbf{v}_{\alpha\beta} e^{-j\theta}. \tag{16}$$

Substituting (14) and (15) into (16) yields

$$\begin{aligned}\mathbf{v^c_{dq}} &= \mathbf{v}_{\alpha\beta}e^{-j\theta} = (V_1 + \mathbf{\Delta v_{dq}})e^{j\theta_1}e^{-j(\theta_1+\Delta\theta)} \\ &= (V_1 + \mathbf{\Delta v_{dq}})e^{-j\Delta\theta}. \end{aligned} \tag{17}$$

Considering the small-signal perturbation $\Delta\theta$, and applying the first-order Taylor expansion, (17) can be approximated as

$$\begin{aligned}\mathbf{v^c_{dq}} &\approx (V_1 + \mathbf{\Delta v_{dq}})(1 - j\mathbf{\Delta}\theta) \\ &= \underbrace{V_1}_{\mathbf{v^c_{dq1}}} + \underbrace{\mathbf{\Delta v_{dq}} - jV_1\mathbf{\Delta}\theta - j\mathbf{\Delta v_{dq}\Delta}\theta}_{\mathbf{\Delta v^c_{dq}}}. \end{aligned} \tag{18}$$

By neglecting the second-order small-signal variation term $\mathbf{\Delta v_{dq}\Delta}\boldsymbol{\theta}$, the small-signal variation of the PCC voltage in the converter *dq*-frame $\mathbf{\Delta v^c_{dq}}$ can be obtained as

$$\mathbf{\Delta v^c_{dq}} \approx \mathbf{\Delta v_{dq}} - jV_1\mathbf{\Delta}\theta. \tag{19}$$

Then, considering the PLL controller shown in Fig. 6, the detected phase variation $\mathbf{\Delta}\theta$ is given by

$$\mathbf{\Delta}\theta = -jG_{pll}(s)\cdot\frac{1}{s}\cdot\mathbf{\Delta v^c_{dq}}. \tag{20}$$

Substituting (19) into (20) yields

$$\mathbf{\Delta}\theta = -j\frac{G_{pll}(s)}{s + G_{pll}(s)V_1}\mathbf{\Delta v_{dq}} \tag{21}$$

which clearly shows that the PLL dynamics in response to a small-signal variation of the PCC voltage.

B. Impact of PLL Dynamics on Modified dq Transformations

Similar to (14)–(18), the modified *dq* transformations used within the *dq*-frame current control can also be linearized as follows:

$$\begin{aligned}\mathbf{i^c_{dq}} &= \mathbf{i}_{\alpha\beta}e^{-j\theta} = (\mathbf{I_{dq1}} + \mathbf{\Delta i_{dq}})e^{-j\mathbf{\Delta}\theta} \\ &\approx (\mathbf{I_{dq1}} + \mathbf{\Delta i_{dq}})(1 - j\Delta\theta) \\ &= \mathbf{I_{dq1}} + \underbrace{\mathbf{\Delta i_{dq}} - j\mathbf{I_{dq1}\Delta}\theta - j\mathbf{\Delta i_{dq}}\Delta\theta}_{\mathbf{\Delta i^c_{dq}}} \end{aligned} \tag{22}$$

where $\mathbf{I_{dq}}1 = I_{d1} + jI_{q1}$ is the steady-state grid current in the converter *dq*-frame, which is also equal to the steady-state grid current in the grid *dq*-frame. By neglecting the second-order small-signal variation term $\Delta\mathbf{i}_{dq}\mathbf{\Delta}\theta$, it can be obtained that

$$\mathbf{\Delta i^c_{dq}} \approx \mathbf{\Delta i_{dq}} - j\mathbf{I_{dq1}\Delta}\theta. \tag{23}$$

Likewise, the *dq*/$\alpha\beta$ transformations used within the *dq*-frame current control can be linearized as follows:

$$\begin{aligned}&\mathbf{u}_{\alpha\beta} = \mathbf{u_{dq}}e^{j\theta_1} = \mathbf{u^c_{dq}}e^{j\theta} \\ &\Rightarrow \mathbf{u_{dq}} = \mathbf{u^c_{dq}}e^{j\mathbf{\Delta}\theta} \approx \left(\mathbf{U_{dq1}} + \Delta\mathbf{u^c_{dq}}\right)(1 + j\Delta\theta) \\ &\Rightarrow \mathbf{\Delta u_{dq}} = \mathbf{u_{dq}} - \mathbf{U_{dq1}} \approx \Delta\mathbf{u^c_{dq}} + j\mathbf{U_{dq1}\Delta}\theta \end{aligned} \tag{24}$$

where $\mathbf{U_{dq1}} = U_{d1} + jU_{q1} \approx V_1$ is the steady-state modulating voltage in the converter *dq*-frame, which is also equal to the steady-state modulating voltage in the grid *dq*-frame.

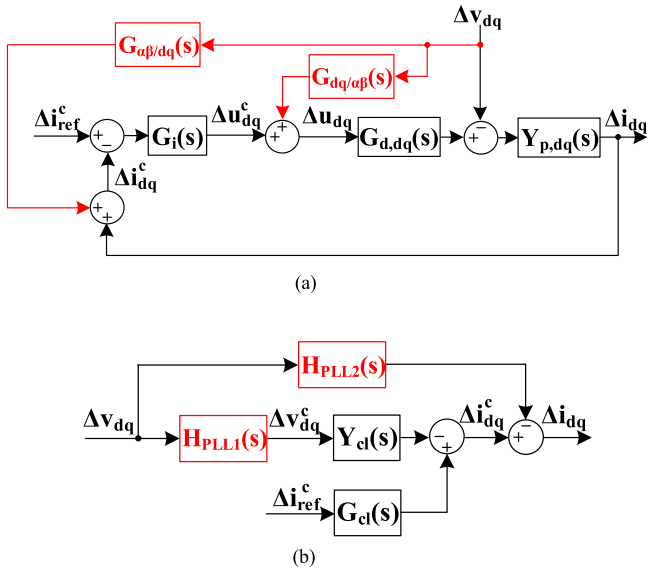

Fig. 8. Block diagram of the grid converter considering the dynamics of complex vector PLL. (a) Original diagram. (b) Equivalent diagram.

Substituting (21) into (23) and (24) leads to

$$\mathbf{\Delta i^c_{dq}} \approx \mathbf{\Delta i_{dq}} - j\mathbf{I_{dq1}\Delta}\theta = \mathbf{\Delta i_{dq}} + \underbrace{\frac{-G_{pll}(s)\cdot\mathbf{I_{dq1}}}{s + G_{pll}(s)V_1}}_{\mathbf{G_{\alpha\beta/dq}(s)}}\mathbf{\Delta v_{dq}} \tag{25}$$

$$\mathbf{\Delta u_{dq}} \approx \Delta\mathbf{u^c_{dq}} + j\mathbf{U}_{dq1}\mathbf{\Delta}\theta = \Delta\mathbf{u^c_{dq}} + \underbrace{\frac{G_{pll}(s)\cdot\mathbf{U}_{dq1}}{s + G_{pll}(s)V_1}}_{\mathbf{G_{dq/\alpha\beta}(s)}}\mathbf{\Delta v_{dq}}. \tag{26}$$

C. SISO Impedance Model With the Symmetrical PLL

According to (25), (26), and Fig. 3, the block diagram of the current control loop with the symmetrical PLL is drawn in Fig. 8(a). $\mathbf{G_{d,dq}(s)}$ and $\mathbf{Y_{p,dq}(s)}$ denote the transfer functions of the digital control delay and *L*-plant in the grid *dq*-frame. Based on the frequency translation between the $\alpha\beta$-frame and *dq*-frame [10], they can be expressed as

$$\mathbf{G_{d,dq}(s)} = \mathbf{G_d(s + j\omega_1)} = e^{-1.5T_s(s+j\omega_1)} \tag{27}$$

$$\mathbf{Y_{p,dq}(s)} = \mathbf{Y_p(s + j\omega_1)} = \frac{1}{(s + j\omega_1)L_f}. \tag{28}$$

Without considering the PLL effect, the closed-loop response of the current control system can be given by

$$\mathbf{\Delta i^c_{dq}} = \underbrace{\frac{\mathbf{T(s)}}{1 + \mathbf{T(s)}}}_{\mathbf{G_{cl}(s)}}\mathbf{\Delta i^c_{ref}} - \underbrace{\frac{\mathbf{Y_{p,dq}(s)}}{1 + \mathbf{T(s)}}}_{\mathbf{Y_{cl}(s)}}\mathbf{\Delta v^c_{dq}} \tag{29}$$

where *T*(*s*) is the open-loop gain of the current control, given by

$$\mathbf{T(s)} = \mathbf{G_i(s)G_{d,dq}(s)Y_{p,dq}(s)}. \tag{30}$$

Considering the PLL effect, additional two items are introduced that modify the original converter admittance, as shown in Fig. 8(b). By applying the equivalent transformation, they can be obtained as

$$\mathbf{H_{PLL1}(s)} = 1 - \mathbf{G_{dq/\alpha\beta}(s)G_{d,dq}(s)} = 1 - \frac{G_{pll}(s)\cdot \mathbf{U_{dq1}}}{s + G_{pll}(s)V_{\mathbf{1}}}$$

$$\mathbf{G_{d,dq}(s)} \approx \frac{s}{s + G_{pll}(s)V_{\mathbf{1}}} \tag{31}$$

$$\mathbf{H_{PLL2}(s)} = \mathbf{G_{\alpha\beta/dq}(s)G_{cl}(s)} = -\frac{G_{pll}(s)\cdot \mathbf{I_{dq1}}}{s + G_{pll}(s)V_{\mathbf{1}}}\mathbf{G_{cl}(s)}. \tag{32}$$

According to Fig. 8(b), the SISO converter admittance model can be expressed as

$$\mathbf{Y_o(s)} = \mathbf{H_{PLL1}(s)}\cdot \mathbf{Y_{cl}(s)} + \mathbf{H_{PLL2}(s)}. \tag{33}$$

VI Stability Analysis and Enhancement Based on SISO Impedance Models

A. SISO Stability Criterion

According to Fig. 1, the grid admittance in the *dq*-frame $Y_g(s)$ can be given by

$$\mathbf{Y_g(s)} = C_g\,(s + j\omega_1) + \frac{1}{L_g\,(s + j\omega_1)}. \tag{34}$$

Meanwhile, with the symmetrical PLL, the frequency coupling effect is removed, and the admittance model of the grid-connected converter $Y_o(s)$ is reduced to SISO transfer function as (33). Therefore, the stability of the grid-converter interactions can be simply justified by the admittance ratio $Y_o(s)/Y_g(s)$. If admittance ratio $Y_o(s)/Y_g(s)$ satisfies the Nyquist stability criterion, then the system will be stable [6]. Moreover, the SISO admittances provide much better physical interpretation than the MIMO admittances, which enables to utilize the SISO impedance shaping methods for stabilizing the power system.

Since it is difficult to change the grid admittance, a practical way is to shape the converter admittance $Y_o(s)$ to make it passive, i.e., to make the phase of $Y_o(s)$ within [–90°, 90°] in a wider frequency range [8].

B. Admittance Characteristics

According to Fig. 8(b), the symmetrical PLL affects the original closed-loop admittance $Y_{cl}(s)$ through the transfer function $H_{PLL1}(s)$, and it can be rewritten by

$$\mathbf{H_{PLL1}(s)} \approx \frac{s}{s + G_{pll}(s)V_1} = \frac{1}{1 + T_{pll}(s)} \tag{35}$$

where $T_{pll}(s)$ is the open-loop gain of the PLL, which is given by

$$T_{pll}(s) = V_1 G_{pll}(s)\frac{1}{s}. \tag{36}$$

Since $T_{pll}(s)$ has a large magnitude within the control bandwidth, $H_{PLL1}(s)$ can be treated as the high-pass filter and its corner frequency is equal to the crossover frequency of $T_{pll}(s)$. Thus, the magnitude of $Y_{cl}(s)$ is reduced by $H_{PLL1}(s)$ within the control bandwidth of the PLL. An additional admittance introduced by symmetrical PLL is given by

$$\mathbf{H_{PLL2}(s)} = -\frac{G_{pll}(s)\cdot \mathbf{I_{dq1}}}{s + G_{pll}(s)V_{\mathbf{1}}}G_{cl}(s) = -\frac{T_{pll}(s)}{1 + T_{pll}(s)}\frac{\mathbf{I_{dq1}}}{V_1}\cdot G_{cl}(s) \tag{37}$$

which can be treated as the negative resistance $-\mathbf{I_{dq1}}/V_1$ within the crossover frequency of $T_{pll}(s)$, and it hence may significantly destabilize the grid-converter interaction.

C. SISO Impedance Shaping to Enhance the Grid Synchronization Stability

To address the adverse effect of $H_{PLL2}(s)$), the SISO impedance shaping technique can be used for stability enhancement. The basic idea is to introduce a virtual positive resistance to cancel the negative resistance introduced by $H_{PLL2}(s)$. Since the converter admittance characteristic at 0 Hz is determined by the direction of current flow (i.e., the inverter operation mode), a high-pass filter should be introduced to avoid the change of the converter admittance at 0 Hz. As a result, the synthesized admittance used for the impedance shaping is given by

$$\mathbf{Y_{shaping}(s)} = -\mathbf{H_{PLL2}(s)}\cdot\frac{s}{s+\omega_L} = \frac{T_{pll}(s)}{1 + T_{pll}(s)}\cdot\frac{\mathbf{I_{dq1}}}{V_1}G_{cl}(s)\cdot\frac{s}{s+\omega_L} \tag{38}$$

where ω_L is the corner frequency of the high-pass filter, and it should be tuned according to frequency responses of SISO converter and of grid impedances to stabilize the whole system. In order to implement this virtual admittance, an additional path with the gain in (38) has to be added from $\mathbf{\Delta v_{dq}}$ to $\mathbf{\Delta i_{dq}}$, as shown in Fig. 9(a). Since $\mathbf{\Delta v_{dq}}$ cannot be measured directly and $\mathbf{\Delta i_{dq}}$ cannot be controlled directly, Fig. 9(a) can be equivalently transformed into Fig. 9(b), where the feedforward function $G_{ff}(s)$ from $\mathbf{\Delta v^c_{dq}}$ to $\mathbf{\Delta i^c_{ref}}$ is given by

$$\mathbf{G_{ff}(s)} = \frac{Y_{shaping}(s)}{H_{PLL1}(s)G_{cl}(s)} \approx T_{pll}(s)\cdot\frac{\mathbf{I_{dq1}}}{V_1}\cdot\frac{s}{s+\omega_L} = \mathbf{I_{dq_1}}\cdot\frac{G_{pll}(s)}{s+\omega_L}. \tag{39}$$

Since $\mathbf{\Delta v^c_{dq}}$ can be measured directly and $\mathbf{\Delta i^c_{ref}}$ is controllable, thus the final implementation of virtual admittance can be depicted by Fig. 9(c).

VII. Experimental Verification

The experimental setup is built to verify the analytical results and the effectiveness of the proposed symmetrical PLL, as shown in Fig. 10. The weak grid is realized by connecting the inductors with a regenerative grid simulator Chroma 61845, the grid-connected converter is implemented based on the Danfoss FC103P11KT11, and the control algorithms are implemented in the dSPACE1007. The circuit parameters are provided in Table I, where the grid voltage is intentionally reduced for a very

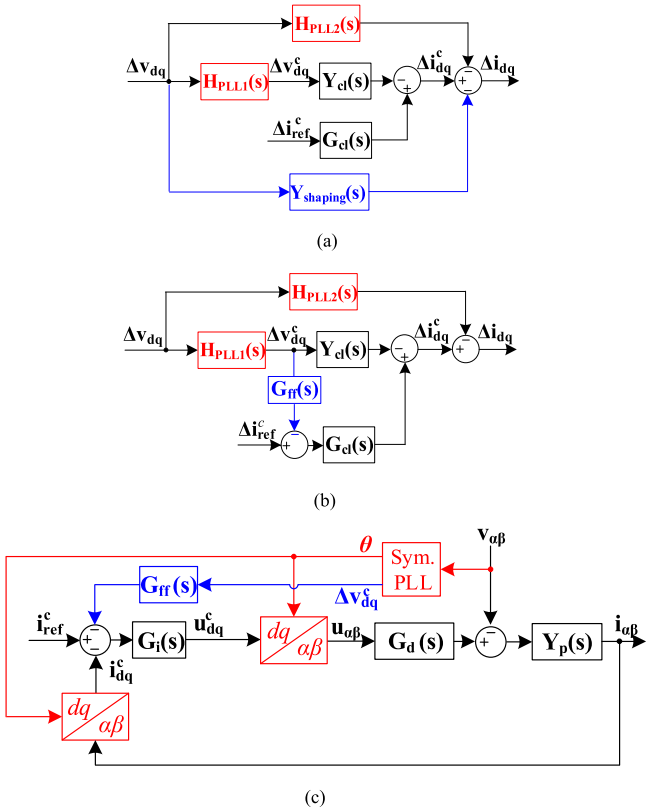

Fig. 9. Impedance shaping scheme. (a) Concept. (b) Equivalent transformation. (c) Implementation.

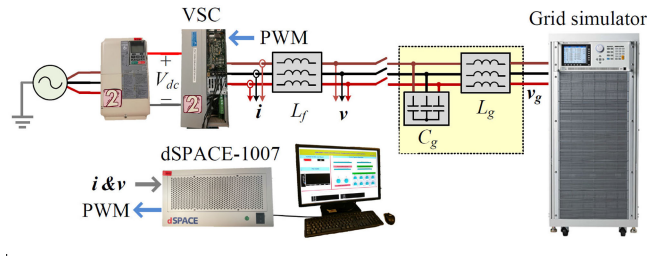

Fig. 10. Experimental setup.

TABLE I
MAIN CIRCUIT PARAMETERS OF VSC

	Parameter	Values
V_{dc}	Input dc-link voltage	600 V
V_1	Rated line to line grid voltage, RMS	130 V
f_1	Grid fundamental frequency	50 Hz
f_{sw}	Inverter switching frequency	10 kHz
f_s	Inverter control sampling frequency	10 kHz
P_n	Rated power	3 kW
L_f	Inverter-side inductor	1 mH
C_g	Grid capacitor	20 μF
L_g	Equivalent grid-side inductor(L_g)	9 mH/1.5 mH
SCR	Short Circuit Ratio	2/12

TABLE II
CONTROL PARAMETERS

	Parameter	Values
k_p	Proportional gain of current controller $G_i(s)$	5.24
k_i	Integral gain of current controller $G_i(s)$	1370
k_{p_p}	Proportional gain of PLL controller $G_{pll}(s)$	0.97
k_{i_p}	Integral gain of PLL controller $G_{pll}(s)$	24.29
ω_L	Corner frequency of impedance shaping function $G_{ff}(s)$	62.8 rad/s

weak grid condition, i.e., low short-circuit ratio (SCR). In this paper, both the current controller $G_i(s)$ and the PLL controller $G_{\rm pll}(s)$ adopts the PI regulator. The used controller parameters are listed in Table II. The cutoff frequencies of the current loop and PLL are 800 and 20 Hz, respectively, when grid impedance is zero. The impact of the grid impedance on the system stability will be analyzed using the impedance-based analysis method.

Since this paper aims at dealing with the frequency coupling and stability issues caused by PLL, the fundamental SRF-PLL is used for comparison rather than various improved PLLs used for better disturbance rejection, fast-tracking performances. With the SRF-PLL, due to the frequency coupling effects, the eigenvalues of the converter-grid impedance matrix ratio has to be utilized to determine the system stability based on the generalized Nyquist stability criterion [7]. As shown in Fig. 11, the system is stable under the stiff grid condition with SCR $=12$, whereas the system is unstable under the weak grid condition with SCR $=2$, and two resonance frequencies should be expected around -40 and 40 Hz in dq-frame. The resonance frequencies will be shifted to 10 and 90 Hz in $\alpha\beta$-frame, respectively, due to 50 Hz frequency shift caused by the $dq/\alpha\beta$ frame transformation [10].

Using the proposed symmetrical PLL, the stability analysis can be greatly simplified with good physical insights. The frequency responses of the SISO converter admittance $Y_o(s)$ and grid admittance $Y_g(s)$ are shown in Fig. 12(a). The system is stable when SCR $=12$ no matter whether the impedance shaping method is used or not. However, the system is unstable without impedance shaping when SCR $=2$. According to the intersection frequency of $Y_o(s)$ and $Y_g(s)$, the resonance frequency should be around 30 Hz in dq-frame and 80 Hz in $\alpha\beta$-frame. This resonance can be stabilized by using the proposed impedance shaping method. Compared with the eigenvalue-based stability analysis for the system with the conventional asymmetrical PLLs, the proposed symmetrical PLL allows a straightforward and design-oriented stability analysis.

Fig. 12(b) shows the influence of the corner frequency ω_L of the high-pass filter in the impedance shaping function (38). It is clear that the corner frequency ω_L changes both the magnitude and phase angle of the $Y_o(s)$ and thereby the system stability margin. To better reveal the impact of the ω_L on the system stability, the Bode diagrams of admittance ratio $Y_o(s)/Y_g(s)$ with different values of ω_L are presented in Fig. 13(a), where the gain margin (GM) and phase margin (PM) can be clearly identified. Moreover, the sensitivity analysis of the GM and PM

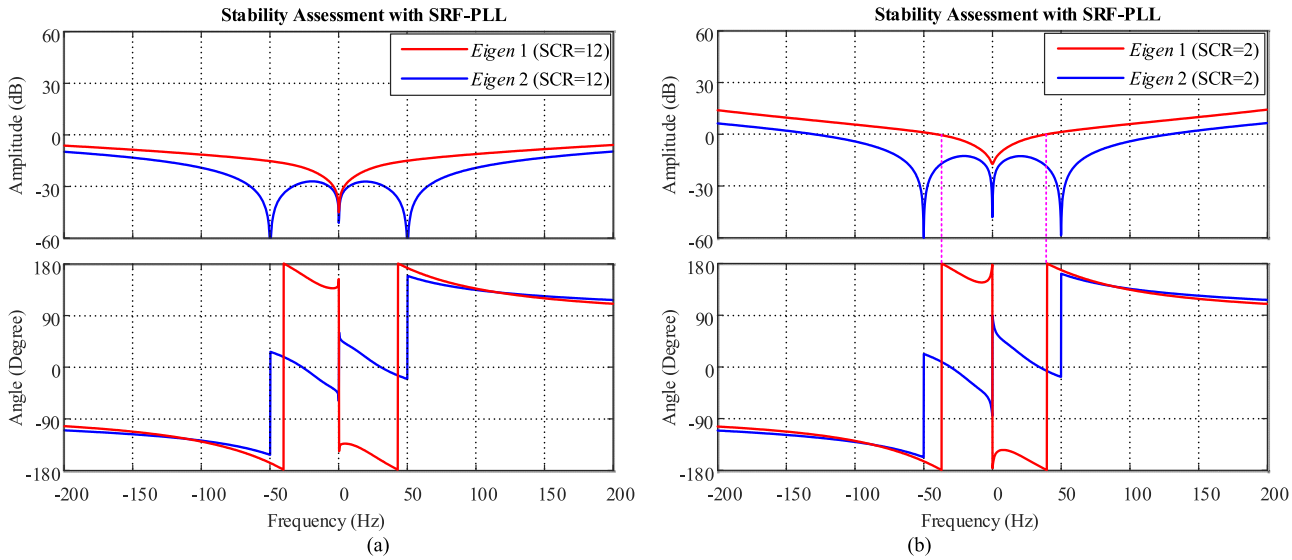

Fig. 11. Frequency response of the eigenvalues of impedance matrix ratio using SRF-PLL. (a) SCR = 12. (b) SCR = 2.

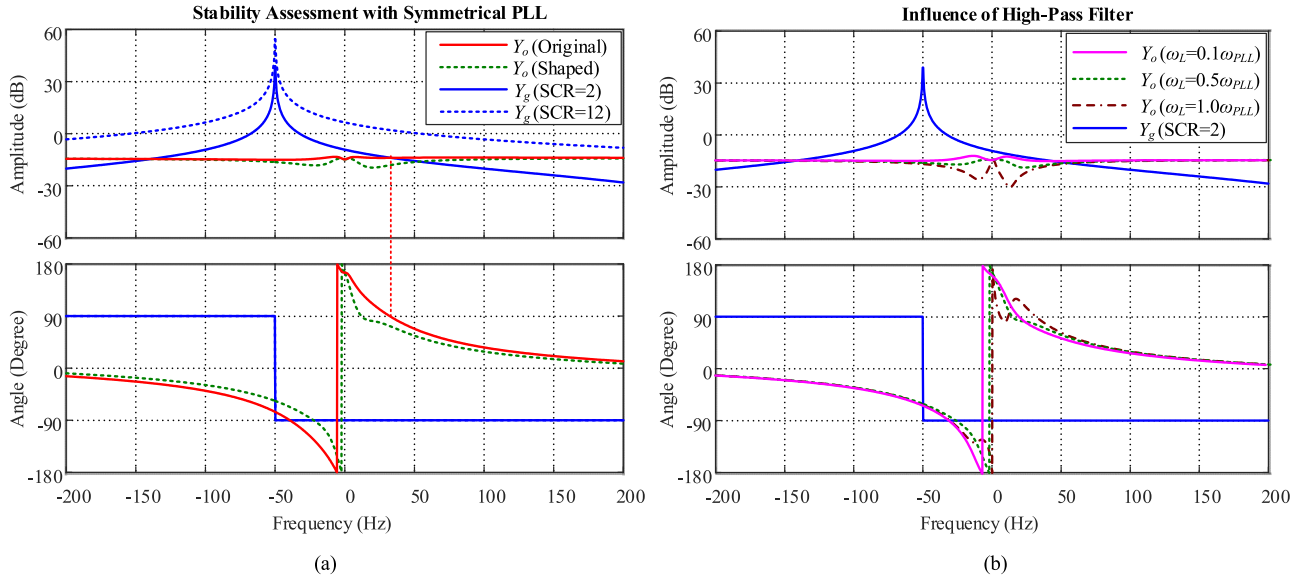

Fig. 12. Frequency response of the SISO admittances $Y_o(s)$ and $Y_g(s)$ using symmetrical PLL. (a) Effect of impedance shaping. (b) Influence of high-pass filter.

are performed against the change of ω_L, as shown in Fig. 13(b), and $\omega_L = 0.5\omega_{PLL}$ is chosen to shape the converter impedance for the relative stability margins of GM = 6 dB and PM = 35°.

In experiments, the SRF-PLL with the same controller parameters is tested first for a comparison with the symmetrical PLL. Fig. 14 shows the experimental waveforms of the grid-connected converter using conventional SRF-PLL. As seen, under the stiff grid condition with SCR = 12, the system is stable. However, under the weak grid condition with SCR = 2.0, although the remote grid voltage v_{gab} is set to be pure sinusoidal, the oscillations can be observed in both the line-to-line PCC voltage v_{ab} and the three-phase grid currents i_a–i_c, which indicates that these oscillations are caused by the stability issues rather than the grid disturbance. Due to the frequency coupling effect of the SRF-PLL, two oscillation frequencies, at approximately 12 and 88 Hz, can be seen in the harmonic spectra of the grid current, which agrees well with the theoretical analysis in Section III.

Fig. 15 shows the experimental waveforms of the grid-connected converter using the proposed symmetrical PLL. Similarly, the system is stable when SCR = 12 and unstable when SCR = 2. However, due to the symmetrical dynamics of PLL, only one oscillation frequency can be observed at 82 Hz in Fig. 15(b), which confirms the correctness of the stability analysis shown in Fig. 13. Meanwhile, the effectiveness of the proposed symmetrical PLL in eliminating the frequency coupling is also verified.

Fig. 16 shows the experimental waveform when SISO impedance shaping is employed to enhance the synchronization stability under the weak grid condition. The system is successfully stabilized, which verifies the effectiveness of the SISO impedance shaping method in Section IV.

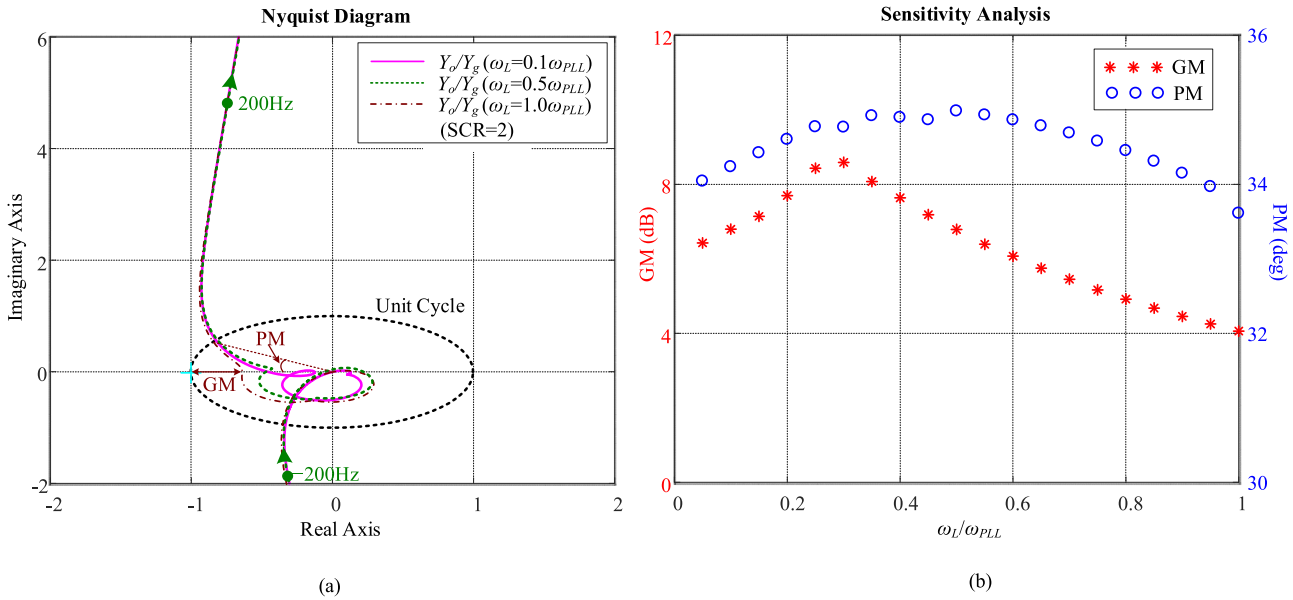

Fig. 13. Stability analysis with different corner frequency ω_L. (a) Nyquist diagrams of admittance ratio $Y_o(s)/Y_g(s)$. (b) Sensitivity of system stable margins.

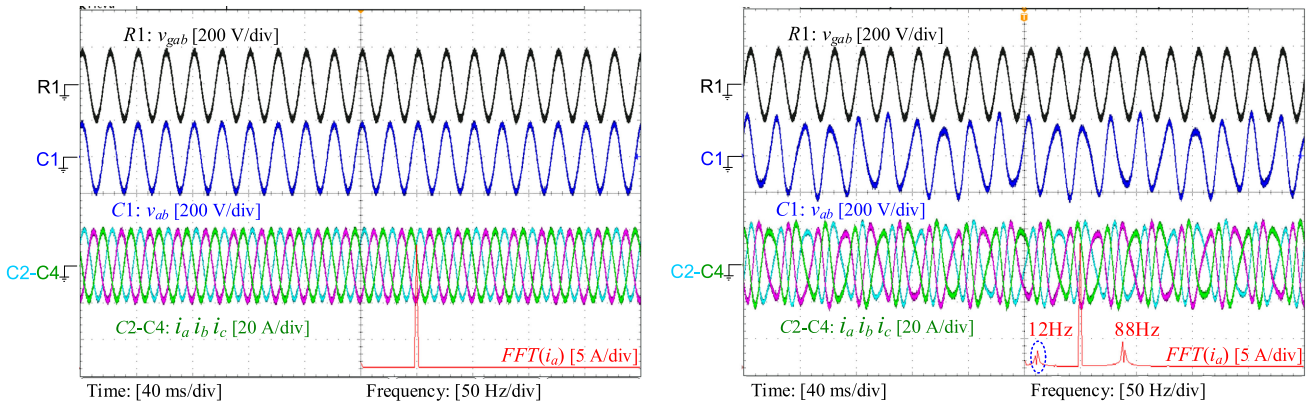

Fig. 14. Experimental waveforms of the grid-connected converter using the conventional SRF-PLL under (a) the stiff grid condition with SCR = 12 and (b) the weak grid condition with SCR = 2.

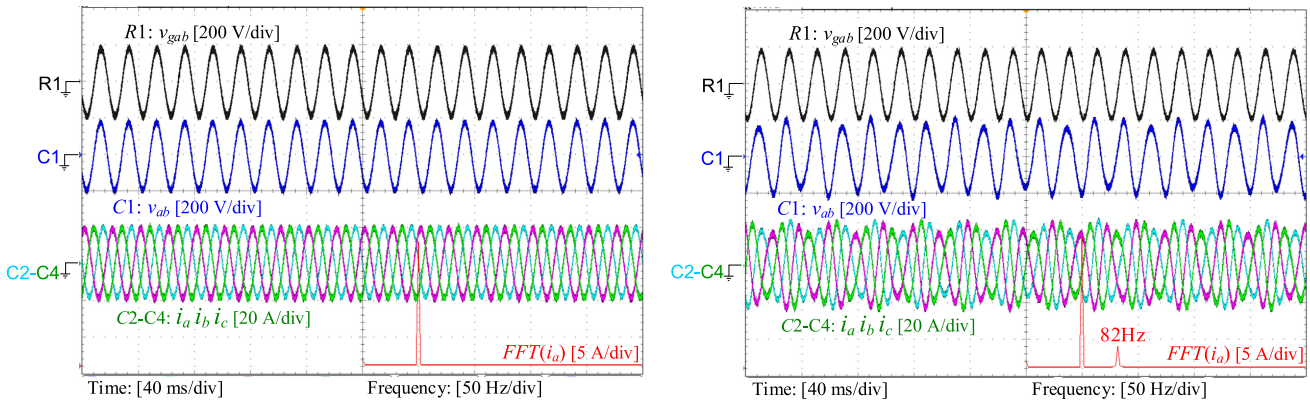

Fig. 15. Experimental waveforms of the grid-connected converter using the symmetrical PLL under (a) the stiff grid condition with SCR = 12 and (b) the weak grid condition with SCR = 2.

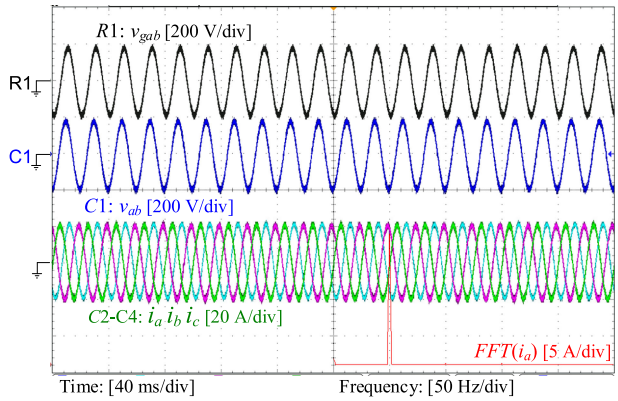

Fig. 16. Experimental waveforms of the grid-connected converter using the symmetrical PLL with SISO impedance shaping under the weak grid condition with SCR = 2.

VIII. Conclusion

In this paper, a symmetrical PLL has been discussed to address the frequency coupling oscillations caused by the grid synchronization loop of grid-connected converters. The small-signal modeling of the symmetrical PLL dynamics has shown that the SISO complex transfer functions can be used to represent the symmetrical PLL. The adverse effects of the PLL can thus be characterized with physical insights and the SISO impedance shaping method can be used to enhance the stability of grid-connected converters under the weak grid condition. Experimental results have confirmed the effectiveness of the proposed symmetrical PLL in terms of the decoupled frequency response and stability enhancement.

References

[1] X. Wang and F. Blaabjerg, "Harmonic stability in power electronic based power systems: Concept, modeling, and analysis," *IEEE Trans. Smart Grid*, vol. 10, no. 3, pp. 2858–2870, May 2019.

[2] J. A. Suul, S. D. Arco, P. Rodríguez, and M. Molinas, "Extended stability range of weak grids with voltage source converters through impedance-conditioned grid synchronization," in *Proc. 11th IET Int. Conf. AC DC Power Transmiss.*, 2015, pp. 1–10.

[3] J. Z. Zhou, H. Ding, S. Fan, Y. Zhang, and A. M. Gole, "Impact of short circuit ratio and phase locked loop parameters on the small signal behavior of a VSC HVDC converter," *IEEE Trans. Power Del.*, vol. 29, no. 5, pp. 2287–2296, Oct. 2014.

[4] T. Messo, J. Jokipii, A. Mäkinen, and T. Suntio, "Modeling the grid synchronization induced negative-resistor-like behavior in the output impedance of a three-phase photovoltaic inverter," in *Proc. IEEE Int. Symp. Power Electron. Distrib. Gener. Syst.*, 2013, pp. 1–7.

[5] X. Wang, F. Blaabjerg, and W. Wu, "Modeling and analysis of harmonic stability in an AC power-electronics-based power system," *IEEE Trans. Power Electron.*, vol. 29, no. 12, pp. 6421–6432, Dec. 2014.

[6] J. Sun, "Impedance-based stability criterion for grid-connected inverters," *IEEE Trans. Power Electron.*, vol. 26, no. 11, pp. 3075–3078, Nov. 2011.

[7] B. Wen, D. Boroyevich, R. Burgos, P. Mattavelli, and Z. Shen, "Analysis of D-Q small-signal impedance of grid-tied inverters," *IEEE Trans. Power Electron.*, vol. 31, no. 1, pp. 675–687, Jan. 2016.

[8] L. Harnefors, M. Bongiorno, and S. Lundberg, "Input-admittance calculation and shaping for controlled voltage-source converters," *IEEE Trans. Ind. Electron.*, vol. 54, no. 6, pp. 3323–3334, Dec. 2007.

[9] M. Cespedes and J. Sun, "Impedance modeling and analysis of grid-connected voltage-source converters," *IEEE Trans. Power Electron.*, vol. 29, no. 3, pp. 1254–1261, Mar. 2014.

[10] X. Wang, L. Harnefors, and F. Blaabjerg, "Unified impedance model of grid-connected voltage-source converters," *IEEE Trans. Power Electron.*, vol. 33, no. 2, pp. 1775–1787, Feb. 2018.

[11] C. Zhang, X. Cai, A. Rygg, and M. Molinas, "Sequence domain SISO equivalent models of a grid-tied voltage source converter system for small-signal stability analysis," *IEEE Trans. Energy Convers.*, vol. 33, no. 2, pp. 741–749, Jun. 2018.

[12] L. Harnefors, "Modeling of three-phase dynamic systems using complex transfer functions and transfer matrices," *IEEE Trans. Ind. Electron.*, vol. 54, no. 4, pp. 2239–2248, Aug. 2007.

[13] M. K. Bakhshizadeh *et al.*, "Couplings in phase domain impedance modelling of grid-connected converters," *IEEE Trans. Power Electron.*, vol. 31, no. 10, pp. 6792–6796, Oct. 2016.

[14] W. Wang *et al.*, "Review of measures to mitigate subsynchronous resonance in power systems," (in Chinese), *Power Syst. Technol.*," vol. 41, no. 4, pp. 1050–1060, Apr. 2017.

[15] X. Yuan, W. Merk, H. Stemmler, and J. Allmeling, "Stationary-frame generalized integrators for current control of active power filters with zero steady-state error for current harmonics of concern under unbalanced and distorted operating conditions," *IEEE Trans. Ind. Appl.*, vol. 38, no. 2, pp. 523–532, Mar./Apr. 2002.

[16] M. Karimi-Ghartemani, H. Karimi, and M. R. Iravani, "A magnitude/phase-locked loop system based on estimation of frequency and in-phase/quadrature-phase amplitudes," *IEEE Trans. Ind. Electron.*, vol. 51, no. 2, pp. 511–517, Apr. 2004.

[17] P. Rodríguez, R. Teodorescu, I. Candela, A. V. Timbus, M. Liserre, and F. Blaabjerg, "New positive-sequence voltage detector for grid synchronization of power converters under faulty grid conditions," in *Proc. 37th IEEE Power Electron. Spec. Conf.*, 2006, pp. 1–7.

[18] P. Rodríguez, A. Luna, I. Candela, R. Mujal, R. Teodorescu, and F. Blaabjerg, "Multiresonant frequency-locked loop for grid synchronization of power converters under distorted grid conditions," *IEEE Trans. Ind. Electron.*, vol. 58, no. 1, pp. 127–138, Jan. 2011.

[19] P. Rodríguez, A. Luna, R. S. Muñoz-Aguilar, I. Etxeberria-Otadui, R. Teodorescu, and F. Blaabjerg, "A stationary reference frame grid synchronization system for three-phase grid-connected power converters under adverse grid conditions," *IEEE Trans. Power Electron.*, vol. 27, no. 1, pp. 99–112, Jan. 2012.

[20] X. Guo, W. Wu, and Z. Chen, "Multiple-complex coefficient-filter-based phase-locked loop and synchronization technique for three-phase grid-interfaced converters in distributed utility networks," *IEEE Trans. Ind. Electron.*, vol. 58, no. 4, pp. 1194–1204, Apr. 2011.

[21] W. Li, X. Ruan, C. Bao, D. Pan, and X. Wang, "Grid synchronization systems of three-phase grid-connected power converters: A complex-vector-filter perspective," *IEEE Trans. Ind. Electron.*, vol. 61, no. 4, pp. 1855–1870, Apr. 2014.

[22] J. Svensson, M. Bongiorno, and A. Sannino, "Practical implementation of delayed signal cancellation method for phase-sequence separation," *IEEE Trans. Power Del.*, vol. 22, no. 1, pp. 18–26, Jan. 2007.

[23] H. E. P. de Souza, F. Bradaschia, F. A. S. Neves, M. C. Cavalcanti, G. M. S. Azevedo, and J. P. de Arruda, "A method for extracting the fundamental-frequency positive- sequence voltage vector based on simple mathematical transformations," *IEEE Trans. Ind. Electron.*, vol. 56, no. 5, pp. 1539–1547, May 2009.

[24] F. A. S. Neves, M. C. Cavalcanti, H. E. P. de Souza, F. Bradaschia, E. J. Bueno, and M. Rizo, "A generalized delayed signal cancellation method for detecting fundamental-frequency positive-sequence three-phase signals," *IEEE Trans. Power Del.*, vol. 25, no. 3, pp. 1816–1825, Jul. 2010.

[25] J. Wang, J. Liang, F. Gao, L. Zhang, and Z. Wang, "A method to improve the dynamic performance of moving average filter-based PLL," *IEEE Trans. Power Electron.*, vol. 30, no. 10, pp. 5978–5990, Oct. 2015.

[26] Y. F. Wang and Y. W. Li, "Grid synchronization PLL based on cascaded delayed signal cancellation," *IEEE Trans. Power Electron.*, vol. 26, no. 7, pp. 1987–1997, Jul. 2011.

[27] M. Karimi-Ghartemani, "A unifying approach to single-phase synchronous reference frame PLLs," *IEEE Trans. Power Electron.*, vol. 28, no. 10, pp. 4550–4556, Oct. 2013.

[28] H. Yi, X. Wang, F. Blaabjerg, and F. Zhuo, "Impedance analysis of SOGI-FLL-based grid synchronization," *IEEE Trans. Power Electron.*, vol. 32, no. 10, pp. 7409–7413, Oct. 2017.

Dongsheng Yang (S'13–M'17) received the B.S., M.S., and Ph.D. degrees in electrical engineering from Nanjing University of Aeronautics and Astronautics, Nanjing, China, in 2008, 2011, and 2016, respectively.

Since 2016, he has been with Aalborg University, Denmark, where he is currently an Assistant Professor with the Department of Energy Technology. His main research interests include modeling, analysis, and control of grid-interactive converters, harmonic and resonance mitigation of large-scale power electronics based power system, impedance measurement technique for real-field harmonic instability assessment, and innovative hardware of power-electronics-based infrastructure for future power grids.

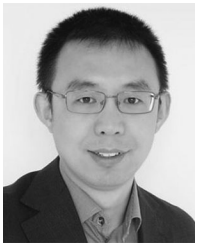

Xiongfei Wang (S'10–M'13–SM'17) received the B.S. degree in electrical engineering from Yanshan University, Qinhuangdao, China, in 2006, the M.S. degree in electrical engineering from Harbin Institute of Technology, Harbin, China, in 2008, and the Ph.D. degree in energy technology from Aalborg University, Aalborg, Denmark, in 2013.

Since 2009, he has been with the Department of Energy Technology, Aalborg University, where he became an Assistant Professor in 2014, an Associate Professor in 2016, a Professor and Research Program Leader for Electronic Power Grid (eGrid) in 2018. His current research interests include modeling and control of grid-interactive power converters, stability and power quality of power electronic based power systems, and active and passive filters.

Dr. Wang serves as an Associate Editor for the IEEE TRANSACTIONS ON POWER ELECTRONICS, the IEEE TRANSACTIONS ON INDUSTRY APPLICATIONS, and the IEEE JOURNAL OF EMERGING AND SELECTED TOPICS IN POWER ELECTRONICS. He was selected into Aalborg University Strategic Talent Management Program in 2016. He was a recipient of six IEEE Prize Paper Awards, the Outstanding Reviewer Award of IEEE TRANSACTIONS ON POWER ELECTRONICS in 2017, and the IEEE PELS Richard M. Bass Outstanding Young Power Electronics Engineer Award in 2018.

Fangcheng Liu received the B.S. degree in electrical engineering from Huazhong University of Science and Technology, Wuhan, China, in 2007, and the Ph.D. degree in electrical engineering from Xi'an Jiaotong University, Xi'an, China, in 2014.

Since 2014, he has been with Huawei, Shanghai, China, where he is currently a Researcher with Watt Laboratory, Central Research Institute. His main research interests include modeling and control of grid-connected converters, and stability of power electronic based power systems.

Kai Xin received the Ph.D. degree in electrical engineering from Huazhong University of Science and Technology, Wuhan, China, in 2007.

He was a Researcher with the Power Conversion System Control Lab, General Electric Global Research Center, Shanghai, China, from 2007 to 2011. Since 2011, he has been with Huawei, Shanghai, China, where he is currently a Technical Expert of Network Energy Product Line and Project Leader of Watt Laboratory, Central Research Institute. His main research interests include grid-connected PV/wind power generation system, and energy conversion techniques and applications.

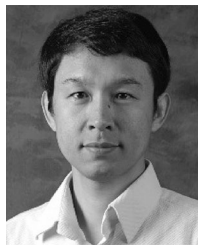

Yunfeng Liu received the Ph.D. degree in electronic engineering from Southeast University, Nanjing, China, in 1999.

He was a Postdoctoral Researcher with the Department of Electrical Engineering, Tsinghua University, Beijing, China, from 1999 to 2001. He was a Visiting Scholar with Virginia Tech-CPES, Virginia, USA, from 2001 to 2003. He was the Senior Researcher with the General Electric Global Research Center (GE GRC), Shanghai, China, and later as the Manager of Power Conversion System Control Lab of GE GRC, from 2003 to 2011. Since 2011, he has been with Huawei, Shanghai, China, where he is currently the Chief Scientist of Network Energy Product Line and Manager of Watt Laboratory, Central Research Institute. His main research interests include high-power semiconductor devices, converter and application in power system, and energy conversion techniques and applications.

Frede Blaabjerg (S'86–M'88–SM'97–F'03) received the Ph.D. degree in electrical engineering from Aalborg University, Aalborg, Denmark, in 1995, and the honoris causa from the University Politehnica Timisoara (UPT), Timişoara, Romania, and Tallinn Technical University (TTU), Tallinn, Estonia.

He was with ABB-Scandia, Randers, Denmark, from 1987 to 1988. He became an Assistant Professor in 1992, an Associate Professor in 1996, and a Full Professor in power electronics and drives in 1998. In 2017, he became a Villum Investigator.

He has authored/coauthored more than 600 journal papers in the fields of power electronics and its applications. He is the co-author of four monographs and editor of ten books in power electronics and its applications. His current research interests include power electronics and its applications, such as in wind turbines, PV systems, reliability, harmonics, and adjustable speed drives.

Prof. Blaabjerg is a recipient of 30 IEEE Prize Paper Awards, the IEEE PELS Distinguished Service Award in 2009, the EPE-PEMC Council Award in 2010, the IEEE William E. Newell Power Electronics Award 2014, and the Villum Kann Rasmussen Research Award 2014. He was the Editor-in-Chief for the IEEE TRANSACTIONS ON POWER ELECTRONICS from 2006 to 2012. He has been a Distinguished Lecturer for the IEEE Power Electronics Society from 2005 to 2007 and for the IEEE Industry Applications Society from 2010 to 2011 as well as 2017 to 2018. Since 2019, he has been serving as the President of the IEEE Power Electronics Society. He is also the Vice-President of the Danish Academy of Technical Sciences.